RSC Applied Polymers

ROYAL SOCIETY OF CHEMISTRY

PAPER

View Article Online
View Journal | View Issue

Check for updates

Cite this: *RSC Appl. Polym.*, 2025, **3**, 370

Composites of azo-linked pyrene-tetraone porous organic polymers as cathodes for lithium-ion batteries†

Heba H. Farrag,[a,b] Eloi Grignon,[a] Alicia M. Battaglia,[a] Jiang Tian Liu[a] and Dwight S. Seferos *[a,c]

Received 22nd October 2024,
Accepted 20th December 2024

DOI: 10.1039/d4lp00320a

rsc.li/rscapplpolym

Organic redox-active polymers offer a potentially sustainable and cost-effective alternative to conventional inorganic electrode materials in rechargeable batteries, yet they struggle with low conductivity and stability. Here, we present a novel porous polymer with dual functionality to overcome these challenges. This polymer incorporates carbonyl (C═O) groups as redox-active units and azo (N═N) groups as linkers, enhancing ion/electron transport and electrode stability by extending conjugation and reducing unused mass. Additionally, carbon nanotubes (CNTs) are integrated into these composites to further increase conductivity, leveraging their exceptional electrical properties. We synthesized azo-linked pyrene-tetraone porous polymers with varying CNT loadings (0%, 30%, and 50%), termed Azo-PTP, Azo-PTP30, and Azo-PTP50, respectively, as cathode materials for organic lithium-ion batteries. Our study demonstrates that Azo-PTP50, with 50% CNTs, achieves a two-fold increase in specific capacity compared to its CNT-free counterpart and maintains superior capacity retention over 200 cycles and 93% retention over 1000 cycles, displaying its enhanced performance and stability.

1. Introduction

The adoption of lithium-ion batteries for energy storage has attracted attention around the globe.[1] However, commercially available lithium-ion batteries rely on transition metal cathodes, which contain elements such as nickel, cobalt, and manganese. This raises environmental concerns due to the generation of CO_2 during the extraction processes of these elements as well as complex and costly post-treatment processes for its disposal and recycling.[2,3] Additionally, these transition metal electrodes are prone to exothermic reactions when overcharged, posing a potential safety risk.[2] In pursuit of sustainable development goals, there is a pressing need for cathode materials that are both performant and environmentally benign. Organic cathode materials offer a promising alternative to transition metal cathodes due to their molecular and structural tunability, low cost, and environmental sustainability.[4–9] Despite promising advancements in organic electrode materials,[10,11] significant challenges remain. These include the dissolution of redox-active species into electrolytes, resulting in reduced stability and efficiency.[12] Furthermore, poor ionic and electronic conductivity limited their overall performance and rate capabilities.[13–15]

One prevalent approach for addressing the solubility challenge of small-molecular organic electrode materials involves utilizing polymeric materials.[16–18] Porous organic polymers (POPs) represent a distinctive category of polymers characterized by the fusion of π-conjugated structures with permanent porosity.[19] POPs have emerged as a robust platform for fabricating functional polymers that demonstrate exceptional performance in various applications, including catalysis,[20] sensors,[21] and CO_2 capture.[22] Due to their unique properties, POPs with designable π frameworks and porous structures are fascinating for developing energy-storage devices.[23–25] However, in the context of battery applications, the inactive and high molecular weight linkers introduced during polymerization decrease the weight ratio of active units in polymer electrode materials, consequently reducing their theoretical capacity. Certain redox-active linkages have been incorporated into the polymer chain to enhance the specific capacity of polymer electrodes.[26–28]

Among these, azo groups (N═N) have emerged as ideal redox-active linkages for porous organic polymers (POPs), offering a combination of structural and electrochemical

[a]Department of Chemistry, University of Toronto, Lash Miller Chemical Laboratories, 80 St. George Street, Toronto, Ontario, M5S 3H6, Canada.
E-mail: dwight.seferos@utoronto.ca
[b]Department of Chemistry, Faculty of Science, Cairo University, Cairo 12613, Egypt
[c]Department of Chemical Engineering and Applied Chemistry, University of Toronto, 200 College Street, Toronto, Ontario, M5S 3E5, Canada

† Electronic supplementary information (ESI) available. See DOI: https://doi.org/10.1039/d4lp00320a

advantages. Their incorporation into the polymer framework enhances the specific capacity of electrodes by serving as active sites that facilitate rapid Li-ion diffusion. Azo linkers also enable structural diversity, allowing for the tailored design of molecular architectures to optimize battery performance. The incorporation of azo groups into molecular structures significantly reduces the HOMO–LUMO gap, thereby enhancing charge transfer properties. When integrated into POPs, azo groups contribute to excellent cycling stability, a rich network of redox-active sites, and tunable pore structures, which enhance lithium-ion storage and transport. Furthermore, the robust framework of azo-linked POPs ensures structural stability, minimizing volume expansion during cycling and supporting long-term durability.[29–33] In 2015, Arab *et al*. synthesized four new porous azo-linked polymers *via* copper(I)-catalyzed oxidative homocoupling of 2D and 3D aniline-like monomers and evaluated their performance for selective CO_2 capture.[34] Building on this, a study was conducted on TPA-based azo-porous organic polymers (Azo-POPs) as cathodes for lithium-ion batteries, demonstrating more than 30% retention of their initial capacity even at a high current density of 20 000 mA g^{-1}.[35] In 2022, Yang and co-workers employed a heterocoupling condensation reaction of tris(4-aminophenyl)amine and *p*-phenylenediamine in the presence of CNTs to prepare NHP@CNT polymers. The NHP@CNTs exhibited a reversible capacity of 145 mA h g^{-1} at 0.05 A g^{-1}, improved rate capability (68.1 mA h g^{-1} at 1.0 A g^{-1}), and enhanced cycling stability, retaining 85 mA h g^{-1} over 160 cycles, outperforming pure NHP cathodes.[36]

Inspired by this previous work, we present the synthesis of novel porous organic polymers featuring an azo group as a linkage and pyrenetetraone (PTO) as a redox-active building block. A key factor in developing high-performance organic cathode materials is the selection of suitable redox-active units. PTO has gained significant attention in electrochemical applications, including lithium-ion batteries (LIBs), due to its four carbonyl groups, which serve as effective redox-active sites capable of multiple reversible reactions.[37,38] These carbonyl groups enable PTO to achieve a high theoretical capacity of 409 mA h g^{-1} for lithium storage,[38] making it a promising candidate for energy storage devices. PTO-based materials have shown potential as cathode materials in LIBs, with PTO-based covalent organic frameworks (COFs) demonstrating high capacities and excellent rate performance.[8,37,39,40]

In this work, we synthesized an azo-linked pyrenetetraone polymer (Azo-PTP) *via in situ* copper(I)-catalyzed oxidative coupling condensation of 2,7-diaminopyrene-4,5,9,10-tetraone (DAPTO) and tris(4-aminophenyl)amine (TAPA). Azo-PTP was tested as a cathode material for lithium-ion batteries (LIBs). Given the inherently poor conductivity of porous organic polymers (POPs), prior studies often integrated POPs with conductive additives such as carbon nanotubes (CNTs).[41,42] To improve the conductivity of the polymer and examine its impact on LIB performance, we varied the carbon nanotube (CNT) content, synthesizing Azo-PTP, Azo-PTP30, and Azo-PTP50 with 0%, 30%, and 50% CNTs by weight, respectively. The Azo-PTP50 composite, containing 50% CNTs, demonstrated the best performance, delivering a capacity of 174 mA h g^{-1} at 50 mA g^{-1} and retaining 98% of its initial capacity after 200 cycles and 93% after 1000 cycles.

2. Experimental section

2.1. Materials

All chemicals were procured from Sigma-Aldrich and Fisher Scientific (TCI America) and utilized without further purification. Multi-walled carbon nanotubes (≥95%) with 30–50 nm outer diameter and 10–20 μm length were purchased from Cheap Tubes Inc.

2.2. Material synthesis

The synthesis of azo-linked pyrenetetraone porous polymers, both with and without CNTs, was conducted *via* a metal-catalyzed oxidative coupling condensation reaction, as outlined in detail in the ESI.†

2.3. Electrode preparation and coin cell assembly

The cathode electrodes were prepared according to the following procedure: PVDF was stirred in *N*-methyl-2-pyrrolidone (NMP) in a small vial equipped with a stirrer bar until completely dissolved. The active material (Azo-PTP, Azo-PTP30, or Azo-PTP50) was then added and stirred for 15 minutes. Subsequently, Super P was added and stirred for another 15 minutes to form a slurry with a concentration of 125 mg mL^{-1}. The slurries were stirred overnight and then sonicated for 6 hours, with stirring every one hour for 5 min to ensure homogeneity. The mass ratio of active materials, carbon black, and PVDF was maintained at 60 : 30 : 10. The slurries were cast onto an aluminum foil current collector (15 μm thickness) using a notch bar with a height of 200 μm. The cast electrodes were air-dried on a hot plate at 120 °C, followed by overnight drying in a vacuum antechamber at 80 °C. The active mass loadings of the electrodes ranged from 0.2 to 0.25 mg cm^{-2}, with detailed values provided in Table S1.† CR2025-type coin cells (MTI Corporation) were assembled within an argon-filled glovebox. Electrodes were cut from the film using a 16 mm electrode punch (DPM Solutions Inc.). Lithium foil (0.38 mm thickness; 16 mm diameter), copper foil (25 μm thickness, 16 mm diameter), and a polypropylene separator (Celgard; 19 mm diameter) were utilized as the counter electrode, current collector, and separator, respectively. The electrolyte consisted of 80 μL of 1 M lithium bis(trifluoromethanesulfonyl)imide (LiTFSI) in a 1 : 1 v/v mixture of 1,3-dioxolane (DOL) and dimethoxyethane (DME). A stainless-steel spacer (0.2 mm thickness) and a spring were included, and the cell was compressed using a digital pressure-controlled electric crimper (MTI Corporation). Prior to analysis, cells were allowed to rest for 18 hours at room temperature to ensure adequate permeation of the electrolyte into the electrodes.

3. Results and discussion

3.1. Synthesis and characterization

Porous organic polymers featuring C═O groups as redox-active moieties and N═N as linking units were synthesized through an oxidative coupling condensation reaction involving monomers containing amino groups. This process entails a stepwise polymerization mechanism, wherein the amino groups undergo a condensation reaction, forming covalent bonds and establishing a polymer network. Similar strategies are commonly employed in organic polymer synthesis, yielding well-defined structures with tailored properties.[34] Incorporating C═O groups introduces redox activity to the material, while the N═N linker participates in π-conjugation, facilitating electron delocalization along the polymer chain and enhancing charge transport.[43] The azo-linked pyrene-tetraone polymers (Azo-PTP) were synthesized through an oxidative coupling condensation reaction involving 2,7-diaminopyrene-4,5,9,10-tetraone (DAPTO) and tris(4-aminophenyl) amine (TAPA), conducted in a mixture of toluene and DMF (1 : 1 v/v) with a CuBr/pyridine catalyst (Fig. 1A). The full synthetic procedures are described in the ESI,† including characterization (Fig. S1–S6†). The successful formation of Azo-PTP was confirmed by ^{13}C CP-MAS solid-state NMR spectroscopy (Fig. S7†), which revealed a characteristic peak at 152.4 ppm corresponding to carbon attached to the azo group (C–N═N), along with a peak at 133.0 ppm representing aromatic carbons.[34]

Next, we examined the possibility of homocoupling between the two monomers, TAPA and DAPTO, both of which possess identical amino groups. Such homocoupling could impact the chemical structure and ultimately influence the electrochemical performance of the final product. Control experiments, conducted under the same conditions as the target polymer synthesis, ruled out significant DAPTO homocoupling, as the product was soluble in DMF, and ^{1}H NMR (Fig. S8†) confirmed the recovery of the starting material.

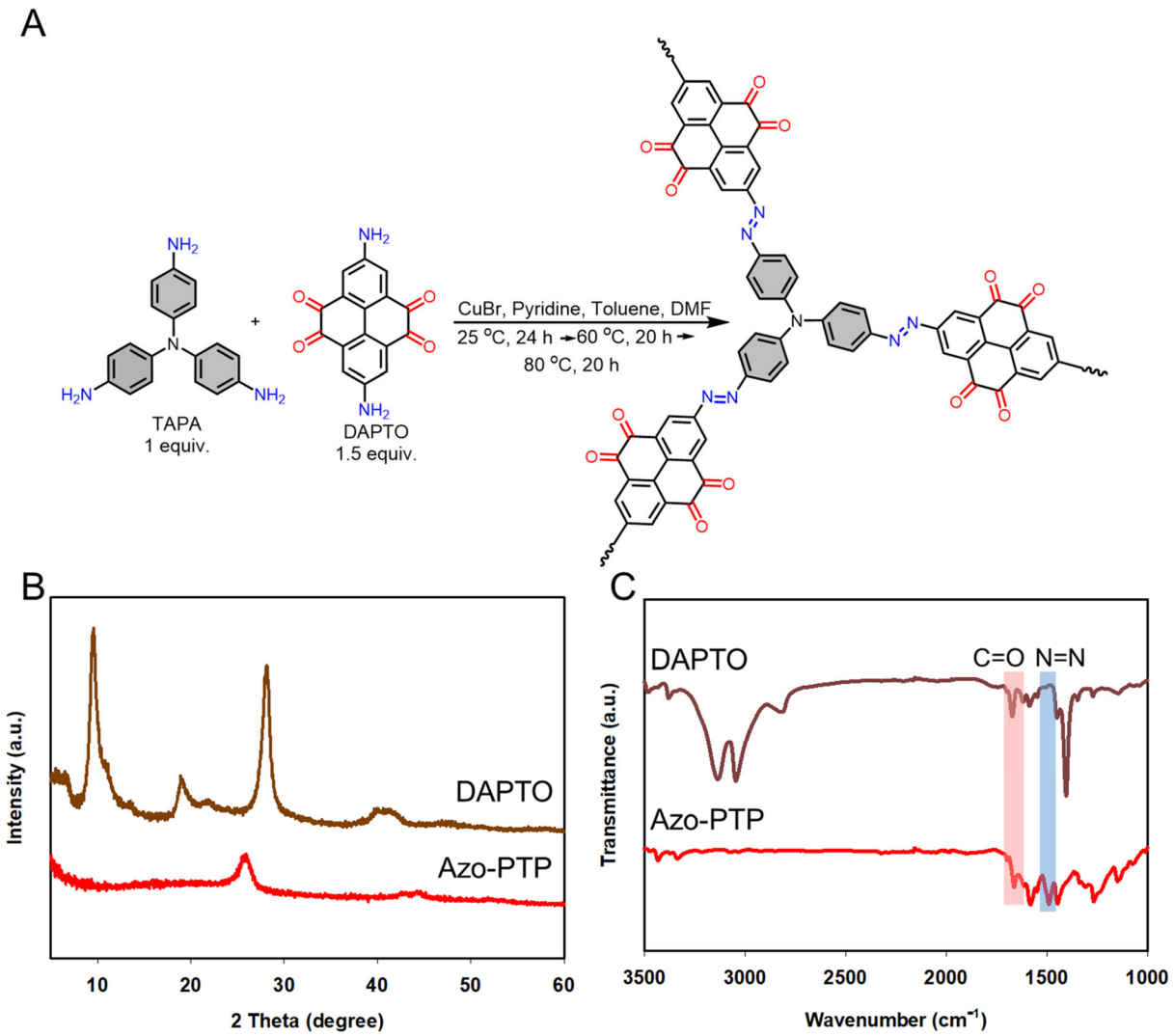

Fig. 1 (A) Synthetic scheme of the azo-linked pyrenetetraone polymer (Azo-PTP), (B) pXRD pattern, and (C) FTIR spectra of DAPTO (brown) and Azo-PTP (red).

However, in the case of TAPA, homocoupling resulted in an insoluble solid, and FTIR analysis (Fig. S9†) showed the disappearance of NH_2 peaks at 3300–3400 cm^{-1}, suggesting that TAPA homocoupling may have occurred during Azo-PTP synthesis, although this remains inconclusive.

Further structural analysis of Azo-PTP and its monomer, DAPTO, was performed using powder X-ray diffraction (pXRD; Fig. 1B). The DAPTO monomer exhibits a diffraction pattern characteristic of a small molecule. However, Azo-PTP shows strong crystal peaks (*d*-spacing = 3.4 Å), suggesting a π–π conjugate stacking architecture.[44] This structural arrangement is conducive to enhanced ion diffusion within the electrode material and accelerated reaction kinetics.[45] Additionally, weaker high-angle diffraction peaks are observed at 42.5° and 44.5°, corresponding to *d*-spacings of 2.1 Å and 2.0 Å, respectively. The formation of Azo-PTP was examined through Fourier transform infrared (FTIR) spectroscopy (Fig. 1C). The successful synthesis of the polymer was corroborated by the disappearance of the N–H vibrational bands, initially present in the starting material (DAPTO), within the 3140–3050 cm^{-1} range, and the emergence of new vibrational bands at 1490 cm^{-1}, corresponding to the azo (N═N) group.[46] The FTIR spectra of DAPTO and the synthesized polymers revealed a carbonyl (C═O) band near 1670 cm^{-1}.

In addition, high-resolution X-ray photoelectron spectroscopy (XPS) was employed to further characterize Azo-PTP, providing detailed information on its chemical composition. The survey spectrum of the polymer confirmed the presence of carbon (C 1s), oxygen (O 1s), and nitrogen (N 1s) components (Fig. S10A†). Notably, the N 1s region displayed two distinct peaks at 400.2 eV and 399.5 eV, which correspond to the C–N and N═N groups within the Azo-PTP chains, respectively (Fig. S10B†).[36] Additionally, the prominent O 1s peak at 531.3 eV primarily indicates the oxygen from the carbonyl group (Fig. S10C†).[29]

To enhance the properties of the synthesized polymer, such as conductivity, thermal stability, and mechanical strength, a composite of Azo-PTP and carbon nanotubes (CNTs) was prepared. Composites with different CNT loading levels were synthesized to assess how varying amounts of CNTs affect the polymer properties and performance in battery applications. Specifically, Azo-PTP30 and Azo-PTP50 composites were synthesized using the same method but with the addition of 30 wt% and 50 wt% of CNTs, respectively. This approach enables a systematic study of the impact of CNT loading on composite characteristics and suitability for battery applications. The formation of Azo-PTP30 and Azo-PTP50 was examined using Fourier transform infrared (FTIR) spectroscopy (Fig. S11†). The successful synthesis of the composites was confirmed by the appearance of new vibrational bands at 1490 cm^{-1}, corresponding to the azo (N═N) group, along with a carbonyl (C═O) band near 1670 cm^{-1}.

The Raman spectra of Azo-PTP, Azo-PTP30, and Azo-PTP50 (Fig. 2A) reveal strong peaks corresponding to N═N bonds at 1448 cm^{-1}.[36] Additionally, two prominent bands, D (1340 cm^{-1}) and G (1578 cm^{-1}), are observed in both Azo-PTP30 and Azo-PTP50, as well as in the CNTs. These bands are indicative of the disordered structure and sp^2-hybridized configuration characteristic of carbon-based materials. This observation further confirms the successful fabrication of the polymer–CNT composites, highlighting the incorporation of CNTs into the polymer matrix.

The thermal stability of Azo-PTP, Azo-PTP30, and Azo-PTP50 was assessed by thermogravimetric analysis (TGA) (Fig. 2B). The porous polymeric materials exhibit enhanced thermal stability with increasing levels of carbon nanotube (CNT) loading.[37] Azo-PTP demonstrates gradual decomposition past 200 °C due to polymer chain dissociation and decarbonization and ultimately retains 35% of its weight at 700 °C. In contrast, Azo-PTP30 and Azo-PTP50 maintain 50% and 61% of their initial weights, respectively, indicating an enhancement in the thermal stability of the composite with the increase in the CNT loading amount.

The permanent porous structure and surface area of the Azo-PTP50 composite were characterized using nitrogen adsorption–desorption isotherms at 77 K. Analysis of the isotherms reveals a type II pattern (Fig. 2C), indicative of mesoporous material characteristics, with a Brunauer–Emmett–Teller (BET) surface area of 343 $m^2\ g^{-1}$. The pore size distribution of the Azo-PTP50 composite, calculated using density functional theory (DFT) fitting with a cylindrical pore model applied to the nitrogen adsorption branch, was approximately 4.0 nm (Fig. 2D). This porous architecture plays a crucial role in enhancing the accessibility of active sites within the polymer matrix and promoting effective contact between the electrolyte and the porous polymer. The uniformly distributed pore channels serve as pathways for the diffusion of Li ions, facilitating ion transport within the electrode material. Additionally, these pores help mitigate large structural changes in the cathode materials during the discharge–charge process, contributing to the overall stability and performance of the battery system.[47]

The morphology of the Azo-PTP, Azo-PTP30, and Azo-PTP50 was characterized using scanning electron microscopy (SEM). The Azo-PTP displays crystalline features, consistent with the observed crystallinity of the prepared polymer, as evidenced by pXRD. In contrast, the Azo-PTP30 and Azo-PTP50 reveal rough surface textures with CNTs fully encapsulated within the polymer shell (Fig. S12†).

3.2. Lithium-storage performance

Following structural characterization, Azo-PTP, Azo-PTP30, and Azo-PTP50 were studied in a lithium-ion half-cell to assess their efficiency as cathode materials. Composite electrodes were fabricated with the polymer (Azo-PTP, Azo-PTP30, or Azo-PTP50) serving as the active material, a conductive carbon additive (Super P), and a PVDF binder in a 60 : 30 : 10 weight ratio using NMP as a solvent. Lithium-ion coin cells (CR2025) were assembled, incorporating composite films as the cathode, lithium metal foil as the anode, and a 1 M LiTFSI solution in a 1 : 1 (v/v) ratio of 1,3-dioxolane to dimethoxy-

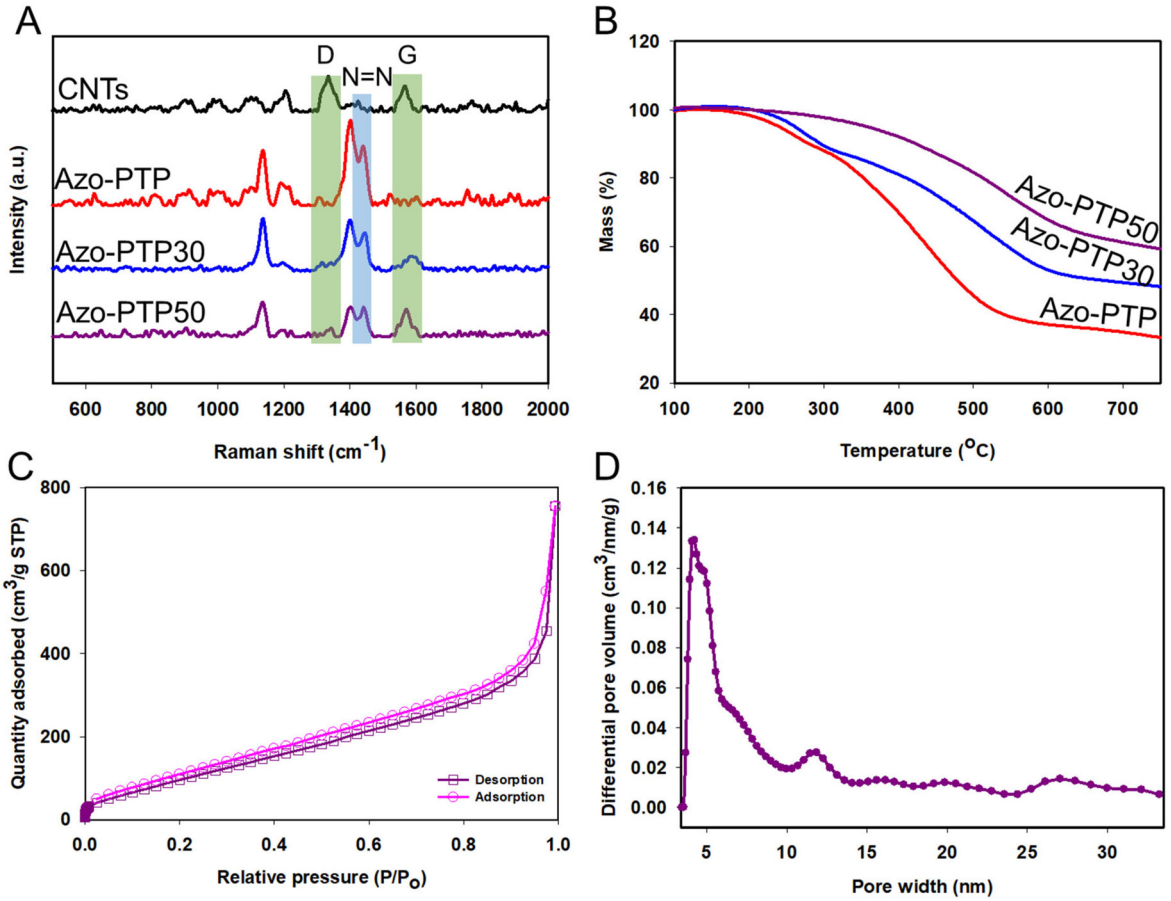

Fig. 2 (A) Raman spectra of CNTs (black), Azo-PTP (red), Azo-PTP30 (blue), and Azo-PTP50 (purple), (B) thermogravimetric analysis curves (TGA) for Azo-PTP (red), Azo-PTP30 (blue), and Azo-PTP50 (purple), (C) N_2 sorption isotherm of Azo-PTP50 (77 K, pink = adsorption; purple = desorption), and (D) pore size distribution (calculated by DFT).

ethane as the electrolyte. To assess the stability and the solubility of the prepared electrode film in the electrolyte, the pristine Azo-PTP composite film was submerged in the electrolyte for over six months. Remarkably, there was no discernible change in the color of the electrolyte even after this extended duration, indicating exceptional stability of the composite material in the selected electrolyte (Fig. S13†).

Based on the literature, materials containing azo groups as redox-active units have been tested as cathodes for lithium-ion batteries in a potential window of 1.0 to 3.5 V.[23,30,36,46,48] Accordingly, the Azo-PTP polymer and its composites were evaluated as cathodes for lithium-ion batteries within the same potential range. The theoretical capacity calculations are provided in Fig. S14 and S15.† The rate performance of the prepared polymers at various current densities (Fig. S16A†) was measured, showing that Azo-PTP50 achieved the highest capacity of 300 mA h g^{-1} at 50 mA g^{-1}, which corresponds to 67% of its theoretical capacity (449 mA h g^{-1}). When the rate was increased to 1000 mA g^{-1}, the capacity decreased to 159 mA h g^{-1}. Upon reinstating the rate to 50 mA g^{-1}, the capacity recovered to its initial value. Azo-PTP30 and Azo-PTP exhibited similar behavior, with initial capacities of 246 and 141 mA h g^{-1} at 50 mA g^{-1}, respectively (Table S2†). Cycling stability was evaluated at a current density of 100 mA g^{-1} over 200 cycles (Fig. S16B†).

The cathodes demonstrated good stability, with a capacity retention of 86%, 87%, and 89% for Azo-PTP, Azo-PTP30, and Azo-PTP50, respectively. Galvanostatic charge/discharge curves were recorded at 50 mA g^{-1} within a potential range of 1.0 to 3.5 V (Fig. S16C†). Despite the high capacity exhibited by the electrodes, particularly Azo-PTP50, the extended discharge plateau raises concerns about the source of this capacity—whether it originates from the active material or from side reactions within the battery.

To investigate the contributions of other components, a control electrode composed of PVDF, CNTs, and SP in a mass ratio of 10% : 60% : 30% was tested in the same electrolyte, yielding a negligible capacity of 23 mA h g^{-1} (Fig. S17†). Despite these investigations, we opted to narrow the potential window to 1.5–3.5 V to further study the behavior and performance of the polymers, focusing on the redox events that did not have a huge hysteresis. By doing so, we exclude the azo group from contributing to the capacity, focusing solely on the carbonyl groups as the redox-active units.

Cyclic voltammetry (CV) was performed on Azo-PTP and its composites with CNTs (Azo-PTP30 and Azo-PTP50) at a scan rate of 0.1 mV s^{-1} within a potential window of 1.5–3.5 V (Fig. 3A). The CV profiles exhibited similar shapes, featuring two broad reduction peaks at around 2.7 and 2.2 V, corresponding to the redox reactions of the carbonyl groups in the DAPTO unit.[37] Charge–discharge tests were performed on Azo-PTP, Azo-PTP30, and Azo-PTP50 within a voltage range of 1.5 to 3.5 V (Fig. 3B). The charge–discharge curves show typical behavior, with the extended plateau observed in the broader potential window (1.0–3.5 V) disappearing. The sloping plateaus in the charge–discharge curves correspond well with the CV profiles, reflecting the reversible oxidation and reduction of the carbonyl groups. Notably, two distinct plateaus are observed in both Azo-PTP and its composites (Azo-PTP30 and Azo-PTP50) at around 2.8 and 2.3 V. The distinction between the two electrochemical processes taking place during cycling in the Azo-PTP, Azo-PTP30, and Azo-PTP50 electrodes becomes

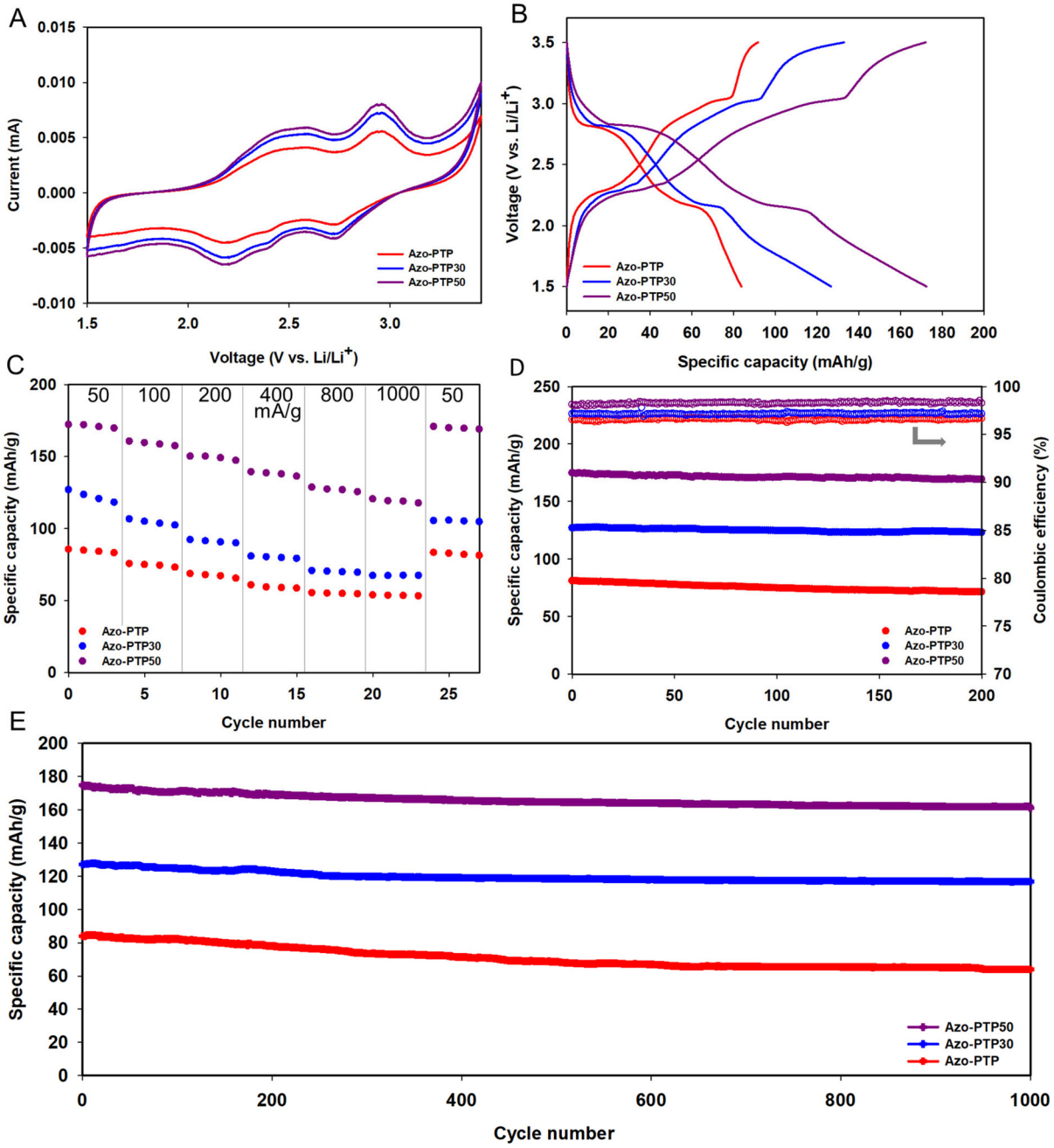

Fig. 3 (A) Cyclic voltammograms (CVs) at a scan rate of 0.1 mV s^{-1}, (B) galvanostatic charge/discharge curves at 50 mA g^{-1}, (C) rate capability, (D) cycling stability at 50 mA g^{-1} for 200 cycles, and (E) long-term cycling stability at 100 mA g^{-1} for 1000 cycles of Azo-PTP (red), Azo-PTP30 (blue), and Azo-PTP50 (purple).

clearer when analyzed using the differential capacity plotted against voltage (Fig. S18†). Azo-PTP delivered a specific capacity of 88 mA h g^{-1} at 50 mA g^{-1}, while the polymer composites exhibited higher capacities, with Azo-PTP50 reaching 174 mA h g^{-1}, corresponding to 78% of its theoretical capacity (224 mA h g^{-1}). Although Azo-PTP50 achieved approximately 78% of the theoretical capacity, this difference may be attributed to TAPA homocoupling during polymer synthesis, which could have altered the DAPTO/TAPA ratio and subsequently affected the measured capacity, as illustrated in the Synthesis and characterization section.

The rate performance of both Azo-PTP and Azo-PTP@CNT composites was evaluated at various current densities ranging from 50 to 1000 mA g^{-1} (Fig. 3C). Initially, Azo-PTP shows a specific capacity of 88 mA h g^{-1} at 50 mA g^{-1}. As the cycling rate increases to 100 mA g^{-1}, the capacity slightly drops to 77 mA h g^{-1}. Further increases in the rate to 200, 400, 800, and 1000 mA g^{-1} result in capacities of 70, 63, 57, and 56 mA h g^{-1}, respectively. In contrast, the Azo-PTP30 electrode begins with a higher capacity of 129 mA h g^{-1} at 50 mA g^{-1} and retains 54% capacity at the highest rate. The Azo-PTP50 electrode exhibits the highest initial capacity of 174 mA h g^{-1} and maintains superior capacities even at increased rates (Table S3†). Notably, the capacity of all electrodes recovers to initial values once the current is reduced back to 50 mA g^{-1}. The electrochemical performance of pure CNTs with carbon black and PVDF was evaluated to assess their individual contributions to the overall electrode performance. Specifically, electrodes comprising CNTs : Super P : PVDF in a mass ratio of 60 : 30 : 10 were tested, revealing a capacity of 2 mA h g^{-1} at

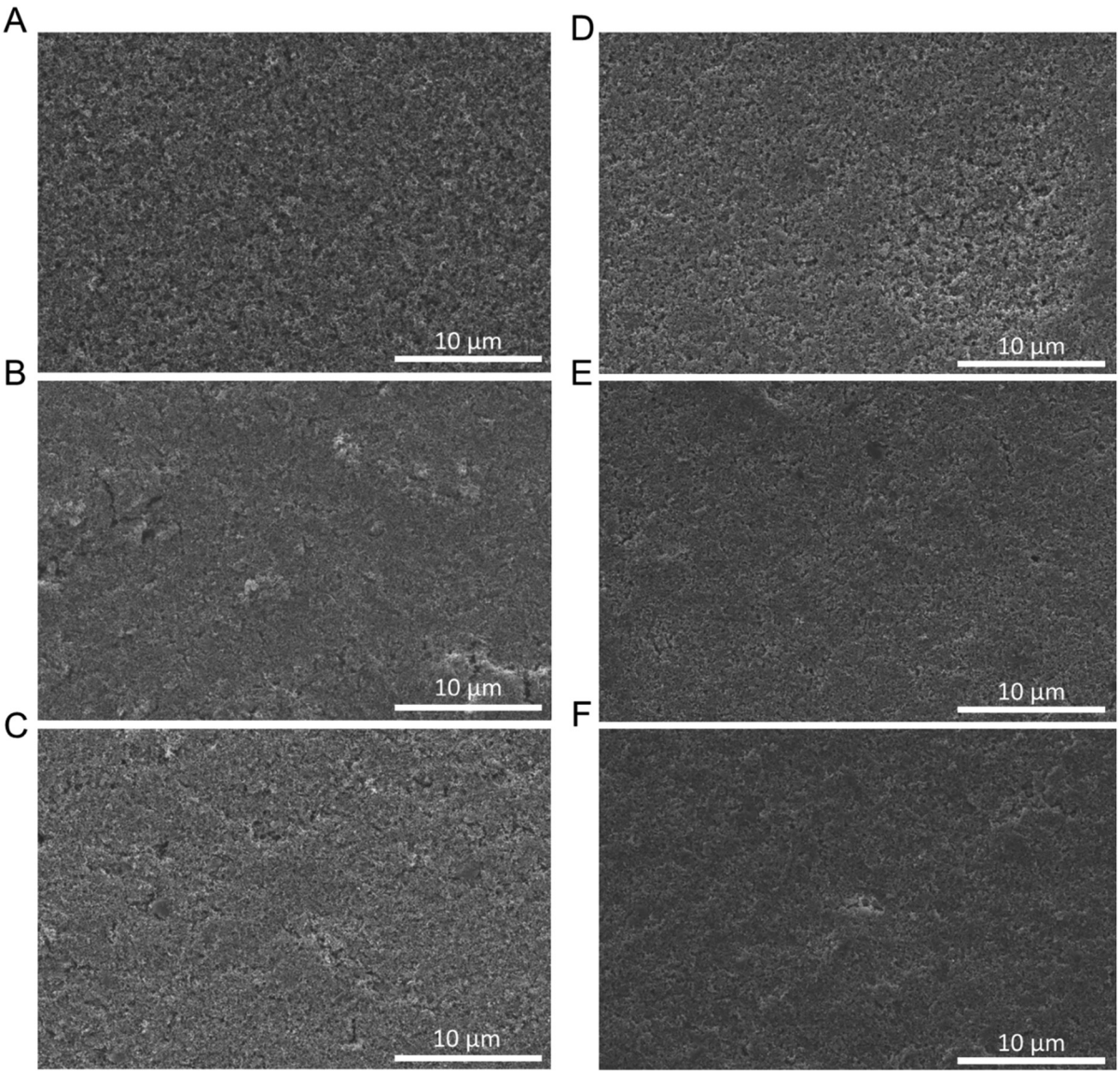

Fig. 4 SEM images of (A) Azo-PTP, (C) Azo-PTP30, (E) Azo-PTP50 pristine electrodes, (B) Azo-PTP, (D) Azo-PTP30, and (F) Azo-PTP50 after 200 cycles.

50 mA g^{-1} (Fig. S19†). This confirms that the contribution of CNTs to the electrode capacity is negligible, and the majority of the capacity is due to the active material. In addition, we investigated the effect of reducing the amount of conductive additive (Super P) on the performance of the Azo-PTP50 electrode. An electrode with an 80 : 10 : 10 composition (active material : Super P : PVDF) was prepared and compared to the 60 : 30 : 10 composition. The rate capability results (Fig. S20†) show that the 80 : 10 : 10 composition starts with a lower initial capacity (~127 mA h g^{-1}) and exhibits a rapid capacity drop upon cycling, reaching ~30 mA h g^{-1} at higher rates. This behavior can be attributed to the formation of an insufficient conductive network due to the reduced Super P content. In contrast, the 60 : 30 : 10 composition delivers a higher initial capacity and superior capacity retention, highlighting the critical role of adequate Super P content in establishing a robust and efficient conductive network. Notably, the 60 : 30 : 10 ratio is widely reported in the literature for similar studies, further supporting its effectiveness.[37]

The cycling stability of the polymers and composites with CNTs was assessed at two current densities, providing a comprehensive view of their long-term performance. At 50 mA g^{-1} for 200 cycles (Fig. 3D), Azo-PTP retains 88% of its initial capacity, while Azo-PTP30 and Azo-PTP50 achieve an impressive capacity retention of 95% and 98%, respectively, with all three formulations exhibiting long-term coulombic efficiencies (CEs) of up to 98%. At a higher current density of 100 mA g^{-1} for 1000 cycles (Fig. 3E), Azo-PTP, Azo-PTP30, and Azo-PTP50 retain 80%, 91%, and 93% of their initial capacities, respectively. These results underscore the role of CNTs in mitigating electrode degradation, enhancing structural integrity, and improving conductivity, making the composites highly promising for lithium-ion battery applications.

The morphologies of the three pristine electrode films and after 200 cycles were imaged using scanning electron microscopy (SEM) (Fig. 4). The SEM images of the Azo-PTP, Azo-PTP30, and Azo-PTP50 pristine films (Fig. 4A, C and E) reveal minimal aggregation and a uniform distribution of components within the electrode films, indicating homogeneity. Notably, the film surfaces exhibit a porous morphology, which could aid in ion diffusion. After 200 cycles, the morphologies of the Azo-PTP, Azo-PTP30, and Azo-PTP50 (Fig. 4B, D and F) reveal that the electrodes remained largely unchanged, with no significant alterations in surface appearance or aggregation, consistent with the stability measurement of the electrodes.

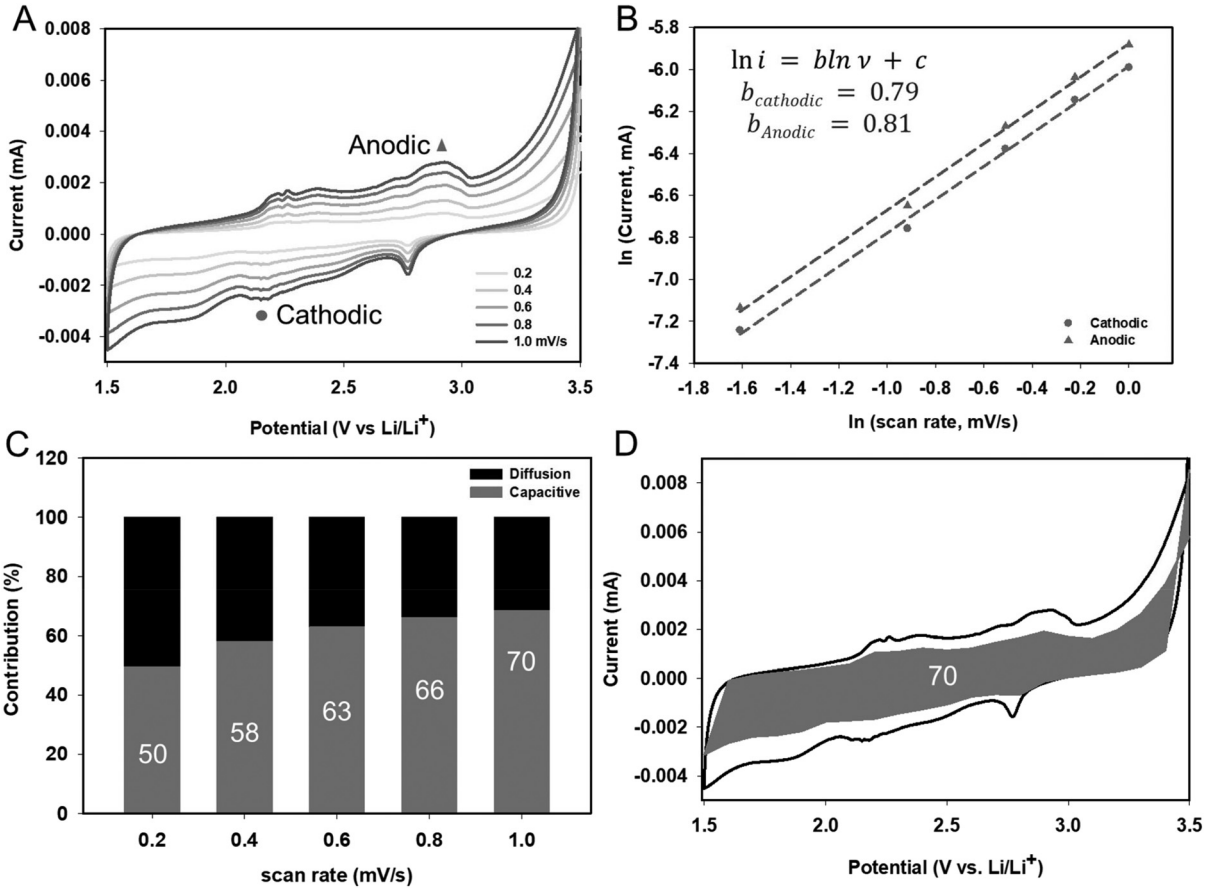

Fig. 5 (A) CV curves of Azo-PTP50 at different scan rates, (B) the corresponding plots ln(*i*) *versus* ln(*ν*) at each redox peak, (C) contribution ratio of pseudocapacitance at various scan rates, and (D) capacitive contribution of Azo-PTP50 at a scan rate of 1 mV s^{-1}.

To relate the electrochemical performance of Azo-PTP and its composites with existing research, Table S4† compares their properties with various organic cathode materials.[29,36–38,46,49,50] Azo-PTP50 demonstrates superior performance, achieving 300 mA h g^{-1} at 50 mA g^{-1} with 89% retention after 200 cycles (1.0–3.5 V), surpassing PBALS and PT-2NO_2 in cycling stability. Within 1.5–3.5 V, it delivers 174 mA h g^{-1} with 93% retention over 1000 cycles, outperforming D-PTO and PT-COF50 in long-term stability. Adjusting the amount of carbon nanotubes (CNTs) in the Azo-PTP materials improves their conductivity and cycling stability. This improvement demonstrates a strong link between the material's structure (the integration of CNTs) and its electrochemical properties (performance as a cathode). As a result, these materials are shown to be effective and long-lasting options for lithium-ion batteries.

The Li^+ storage mechanism of Azo-PTP50, which exhibits the highest performance as a cathode material in lithium-ion batteries, was further investigated. Characterization of cyclic voltammetry (CV) curves at various scan rates (Fig. 5A) shows notable shifts in both cathodic and anodic peaks towards lower and higher potentials with increasing scan rates. This behavior suggests an amplified degree of polarization.[29,50] The electrochemical behavior was further analyzed using the Dunn method to calculate diffusive and capacitive contributions according to the equation $i = av^b$.[50] From the ln–ln plot of peak current and scan rate, b values of 0.81 and 0.79 were calculated for the anodic and cathodic processes, respectively (Fig. 5B). With b values ranging from 0.5 to 1, there is an indication of a hybrid contribution from both capacitive and diffusion processes. Moreover, the capacitive contribution at different scan rates was quantified using the equation $i = k_1v + k_2v^{1/2}$, revealing an increase from 49.5% to 68.6% as the scan rate escalated from 0.2 to 1 mV s^{-1} (Fig. 5C). These findings underscore the capacitive nature of Li^+ storage in Azo-PTP50, particularly at high rates. At a scan rate of 1 mV s^{-1} (Fig. 5D), the capacitive contribution is clearly represented.

Finally, the charge-transfer properties of the polymers and composites were studied using electrochemical impedance spectroscopy (EIS). The cells were first cycled ten times at 50 mA g^{-1} to allow SEI formation and complete electrolyte permeation, followed by a ten-hour rest period to stabilize before taking impedance measurements at open-circuit voltage. The EIS data were plotted as Nyquist plots for all electrodes (Fig. S20†). The high-frequency region represents charge transfer resistance, while the Warburg tail in the low-frequency region indicates ion diffusion.[51,52] The Nyquist plots show a decrease in charge transfer resistance for the Azo-PTP50 electrode compared to Azo-PTP and Azo-PTP30. Lower resistance indicates faster electrochemical kinetics, further supporting the superior battery performance of Azo-PTP50.

4. Conclusion

In summary, novel porous organic polymers were synthesized and evaluated as cathode materials for organic lithium-ion batteries. The synthetic strategy enabled the incorporation of azo linkers, resulting in polymers with dual functional groups (C═O and N═N). Composites of these polymers, designated as Azo-PTP, Azo-PTP30, and Azo-PTP50, were prepared with varying CNT contents (0%, 30%, and 50% by weight, respectively). Initially, the polymers were tested within a potential window of 1.0–3.5 V, which is typical for azo-containing redox molecules. However, due to extended plateaus and poor voltage efficiency observed in the discharge curves, the potential window was narrowed to 1.5–3.5 V, focusing on PTO as the primary redox-active moiety. This adjustment led to superior performance, with Azo-PTP50 delivering a capacity of 174 mA h g^{-1} and achieving 93% capacity retention after 1000 cycles at 50 mA g^{-1}. The exceptional electrochemical performance is attributed to the synergistic effects of the highly conductive CNT cores and the redox-active carbonyl groups within the polymer structure, which help mitigate the impact of the material's limited intrinsic electronic conductivity. These findings highlight the promise of Azo-PTP50 as a sustainable, metal-free electrode material for next-generation, low-cost, high-performance lithium-ion batteries. We anticipate that this work will inspire further research into the synthesis of porous polymers with azo linkers, offering valuable insights into the development of innovative organic building blocks for future energy storage technologies.

Author contributions

The manuscript was written through contributions of all authors. All authors have given approval to the final version of the manuscript.

Data availability

The authors confirm that the data supporting the findings of this study are available within the article and/or its ESI.†

Conflicts of interest

The authors declare no competing financial interest.

Acknowledgements

This work was supported by the National Sciences and Engineering Research Council of Canada (NSERC), the Canadian Foundation for Innovation, and the Ontario Research Fund. H.H.F. is grateful to the Ministry of Higher Education and Scientific Research, Egypt, A.M.B. for an Ontario Graduate Scholarship, E.G. for an NSERC CGS-D, and J.T.L. for an NSERC PGS-D. We acknowledge the support of the Government of Canada's New Frontiers in Research Fund (NFRF), CANSTOREnergy project NFRFT-2022-00197. The authors thank Dr. Darcy Burns for solid-state NMR measurements; Dr. Peter Broderson for XPS measurements; Dr. Ilya

Gourevich for help with SEM measurements; Prof. Chul Park and Maryam Fashandi for BET measurements; and Dr. Harrison Mills and Bryton Varju for helpful discussions.

References

1 M. Armand and J.-M. Tarascon, *Nature*, 2008, **451**, 652–657.
2 L. Croguennec and M. R. Palacin, *J. Am. Chem. Soc.*, 2015, **137**, 3140–3156.
3 J. Kim, Y. Kim, J. Yoo, G. Kwon, Y. Ko and K. Kang, *Nat. Rev. Mater.*, 2022, **8**, 54–70.
4 T. B. Schon, B. T. McAllister, P.-F. Li and D. S. Seferos, *Chem. Soc. Rev.*, 2016, **45**, 6345–6404.
5 J. J. Shea and C. Luo, *ACS Appl. Mater. Interfaces*, 2020, **12**, 5361–5380.
6 Q. Zhao, Y. Lu and J. Chen, *Adv. Energy Mater.*, 2017, **7**, 1601792.
7 J. Heiska, M. Nisula and M. Karppinen, *J. Mater. Chem. A*, 2019, **7**, 18735–18758.
8 T. Sun, J. Xie, W. Guo, D. Li and Q. Zhang, *Adv. Energy Mater.*, 2020, **10**, 1904199.
9 Y. Lu and J. Chen, *Nat. Rev. Chem.*, 2020, **4**, 127–142.
10 Y. Liang, P. Zhang and J. Chen, *Chem. Sci.*, 2013, **4**, 1330.
11 Y. Morita, S. Nishida, T. Murata, M. Moriguchi, A. Ueda, M. Satoh, K. Arifuku, K. Sato and T. Takui, *Nat. Mater.*, 2011, **10**, 947–951.
12 A. N. Davis, K. Parui, M. M. Butala and A. M. Evans, *Nanoscale*, 2024, **16**, 10142–10154.
13 C. Heubner, K. Nikolowski, S. Reuber, M. Schneider, M. Wolter and A. Michaelis, *Batteries Supercaps*, 2021, **4**, 268–285.
14 J. T. Liu, E. Grignon, A. M. Battaglia, M. Imran, C. Copeman, H. A. Mills, A. J. Howarth, E. H. Sargent and D. S. Seferos, *Chem. Mater.*, 2023, **35**, 9692–9701.
15 A. Banerjee, N. Khossossi, W. Luo and R. Ahuja, *J. Mater. Chem. A*, 2022, **10**, 15215–15234.
16 Y. Liang, Y. Jing, S. Gheytani, K.-Y. Lee, P. Liu, A. Facchetti and Y. Yao, *Nat. Mater.*, 2017, **16**, 841–848.
17 Z. Li, J. Tan, X. Zhu, S. Xie, H. Fang, M. Ye and J. Shen, *Energy Storage Mater.*, 2022, **51**, 294–305.
18 A. N. Davis, K. Parui, A. M. M. Hasan, L. A. Pineda, J. D. Langhout, K. A. Treaster, M. M. Butala and A. M. Evans, *J. Mater. Chem. A*, 2024, **12**, 28874–28881.
19 J. Jiang, F. Su, A. Trewin, C. D. Wood, N. L. Campbell, H. Niu, C. Dickinson, A. Y. Ganin, M. J. Rosseinsky, Y. Z. Khimyak and A. I. Cooper, *Angew. Chem.*, 2007, **119**, 8728–8732.
20 D.-H. Yang, Y. Tao, X. Ding and B.-H. Han, *Chem. Soc. Rev.*, 2022, **51**, 761–791.
21 S. Wang, H. Li, H. Huang, X. Cao, X. Chen and D. Cao, *Chem. Soc. Rev.*, 2022, **51**, 2031–2080.
22 K. S. Song, P. W. Fritz and A. Coskun, *Chem. Soc. Rev.*, 2022, **51**, 9831–9852.
23 J. Wang, C. S. Chen and Y. Zhang, *ACS Sustainable Chem. Eng.*, 2018, **6**, 1772–1779.
24 D. Luo, M. Li, Q. Ma, G. Wen, H. Dou, B. Ren, Y. Liu, X. Wang, L. Shui and Z. Chen, *Chem. Soc. Rev.*, 2022, **51**, 2917–2938.
25 X. Liu, C.-F. Liu, S. Xu, T. Cheng, S. Wang, W.-Y. Lai and W. Huang, *Chem. Soc. Rev.*, 2022, **51**, 3181–3225.
26 W. Choi, D. Harada, K. Oyaizu and H. Nishide, *J. Am. Chem. Soc.*, 2011, **133**, 19839–19843.
27 W. Huang, Z. Zhu, L. Wang, S. Wang, H. Li, Z. Tao, J. Shi, L. Guan and J. Chen, *Angew. Chem., Int. Ed.*, 2013, **52**, 9162–9166.
28 A. Vlad, K. Arnould, B. Ernould, L. Sieuw, J. Rolland and J.-F. Gohy, *J. Mater. Chem. A*, 2015, **3**, 11189–11193.
29 C. Luo, X. Ji, S. Hou, N. Eidson, X. Fan, Y. Liang, T. Deng, J. Jiang and C. Wang, *Adv. Mater.*, 2018, **30**, 1706498.
30 C. Wu, M. Hu, X. Yan, G. Shan, J. Liu and J. Yang, *Energy Storage Mater.*, 2021, **36**, 347–354.
31 A. A. Pavlovskii, K. Pushnitsa, A. Kosenko, P. Novikov and A. A. Popovich, *Materials*, 2022, **16**, 177.
32 M. Jia, L. Zhang and Q. Yuan, *Molecules*, 2023, **28**, 5953.
33 N. Singh, M. Arish, P. Kumar, A. Rub and U. Riaz, *Sci. Rep.*, 2020, **10**, 57.
34 P. Arab, E. Parrish, T. İslamoğlu and H. M. El-Kaderi, *J. Mater. Chem. A*, 2015, **3**, 20586–20594.
35 S. Ahmed, K. Amin, M. Younis, Z. Wei and M.-H. Huang, *ACS Appl. Energy Mater.*, 2023, **6**, 10674–10681.
36 X. Ma, Y. Dong, C. He, N. Jiang and Y. Yang, *Mater. Adv.*, 2022, **3**, 5818–5825.
37 H. Gao, A. R. Neale, Q. Zhu, M. Bahri, X. Wang, H. Yang, Y. Xu, R. Clowes, N. D. Browning, M. A. Little, L. J. Hardwick and A. I. Cooper, *J. Am. Chem. Soc.*, 2022, **144**, 9434–9442.
38 L. Ueberricke, F. Mildner, Y. Wu, E. Thauer, T. Wickenhäuser, W.-S. Zhang, Y. Vaynzof, S. M. Elbert, R. R. Schröder, R. Klingeler and M. Mastalerz, *Mater. Adv.*, 2023, **4**, 1604–1611.
39 L. Yang and N. Huang, *J. Polym. Sci.*, 2022, **60**, 2225–2238.
40 H. Gao, Q. Zhu, A. R. Neale, M. Bahri, X. Wang, H. Yang, L. Liu, R. Clowes, N. D. Browning, R. S. Sprick, M. A. Little, L. J. Hardwick and A. I. Cooper, *Adv. Energy Mater.*, 2021, **11**, 2101880.
41 T. Zhou, Y. Yuan, L. Xiao, W. Ding, Y. Wang and L.-P. Lv, *Nanomaterials*, 2024, **14**, 1388.
42 F. Xu, S. Jin, H. Zhong, D. Wu, X. Yang, X. Chen, H. Wei, R. Fu and D. Jiang, *Sci. Rep.*, 2015, **5**, 8225.
43 S. Zhang, F. Xing, L. Chen, X. Wang and X. He, *Chem. Mater.*, 2022, **34**, 9031–9041.
44 C. Li, J. Yang, P. Pachfule, S. Li, M.-Y. Ye, J. Schmidt and A. Thomas, *Nat. Commun.*, 2020, **11**, 4712.
45 Y. Lin, H. Cui, C. Liu, R. Li, S. Wang, G. Qu, Z. Wei, Y. Yang, Y. Wang, Z. Tang, H. Li, H. Zhang, C. Zhi and H. Lv, *Angew. Chem., Int. Ed.*, 2023, **62**, e202218745.
46 Z. Sun, H. Yao, J. Li, B. Liu, Z. Lin, M. Shu, H. Liu, S. Zhu and S. Guan, *ACS Appl. Mater. Interfaces*, 2023, **15**, 42603–42610.
47 Z. Ba, Z. Wang, M. Luo, H. Li, Y. Li, T. Huang, J. Dong, Q. Zhang and X. Zhao, *ACS Appl. Mater. Interfaces*, 2020, **12**, 807–817.
48 T. Shimizu, N. Tanifuji and H. Yoshikawa, *Angew. Chem., Int. Ed.*, 2022, **61**, e202206093.

49 Z. Sun, H. Liu, M. Shu, Z. Lin, B. Liu, Y. Li, J. Li, T. Yu, H. Yao, S. Zhu and S. Guan, *ACS Appl. Mater. Interfaces*, 2022, **14**, 36700–36710.
50 Q. Li, H. Wang, H. Wang, Z. Si, C. Li and J. Bai, *ChemSusChem*, 2020, **13**, 2449–2456.
51 E. Grignon, A. M. Battaglia, J. T. Liu, B. T. McAllister and D. S. Seferos, *ACS Appl. Mater. Interfaces*, 2023, **15**, 45345–45353.
52 G. Gao, X. Wang, L. Chen, T. Baumgartner and X. He, *Chem. Mater.*, 2021, **33**, 4596–4605.